Topological defects produce kinks in biopolymer filament bundles

Valentin M. Slepukhin[a,1], Maximilian J. Grill[b], Qingda Hu[c,d], Elliot L. Botvinick[c,d,e], Wolfgang A. Wall[b], and Alex J. Levine[a,f,g]

[a]Department of Physics and Astronomy, University of California, Los Angeles, CA 90095-1596; [b]Institute for Computational Mechanics, Technical University of Munich, 80333 Munich, Germany; [c]Department of Biomedical Engineering, University of California, Irvine, CA 92697-2730; [d]Center for Complex Biological Systems, University of California, Irvine, CA 92697-2280; [e]Beckman Laser Institute, University of California, Irvine, CA 92697-2730; [f]Department of Chemistry and Biochemistry, University of California, Los Angeles, CA 90095-1596; and [g]Department of Biomathematics, University of California, Los Angeles, CA 90095-1596

Edited by Yitzhak Rabin, Bar-Ilan University, Ramat-Gan, Israel, and accepted by Editorial Board Member Mehran Kardar February 27, 2021 (received for review November 24, 2020)

Bundles of stiff filaments are ubiquitous in the living world, found both in the cytoskeleton and in the extracellular medium. These bundles are typically held together by smaller cross-linking molecules. We demonstrate, analytically, numerically, and experimentally, that such bundles can be kinked, that is, have localized regions of high curvature that are long-lived metastable states. We propose three possible mechanisms of kink stabilization: a difference in trapped length of the filament segments between two cross-links, a dislocation where the endpoint of a filament occurs within the bundle, and the braiding of the filaments in the bundle. At a high concentration of cross-links, the last two effects lead to the topologically protected kinked states. Finally, we explore, numerically and analytically, the transition of the metastable kinked state to the stable straight bundle.

semiflexible filaments | bundles | topological defects | elasticity

Semiflexible biopolymer filaments, that is, stiff filaments whose thermal persistence length is comparable to their length, form most of the structural elements within cells and in the extracellular matrix surrounding them in tissues. Common intracellular examples include the F-actin and intermediate filaments forming the cytoskeleton, while the extracellular matrix making up most tissues is composed of other stiff filamentous structures, such as collagen and elastin fibers. The three-dimensional (3D) structure of these fiber networks is typically fixed by a variety of specific cross-linking proteins. On a smaller scale, these filaments often share a similar structural motif—they form bundles of nearly aligned filaments, which are often densely cross-linked along their contours.

While bundles might be regarded merely as new and thicker (thus stiffer) filaments, this analysis is inadequate in detail. For instance, bundle bending mechanics can dramatically differ from those of a simple filament because, by having extra degrees of freedom associated with sliding one constituent filament relative to another within the bundle, the bundle acquires a length-dependent effective bending modulus (1, 2). These internal degrees of freedom also suggest that a nearly parallel group of filaments, when quenched into a bundle by the addition of cross-linking agents, may end up in one of many metastable states in which cross-linking traps a defect, that is, a long-lived structure distinct from the elastic ground state of straight, parallel, and densely cross-linked filaments. We focus on these defected, metastable states and their effect on the low-energy configurations of the bundle. Specifically, we show that there are three types of defects, two of which correspond to topological defects in the bundle's unstressed state—braids and dislocations. These and a third form of trapped length (loops) are all long-lived structures due to cross-linking.

As a result of these structural defects within the bundle, the elastic reference state is no longer straight, even though straight filament configurations are individually the lowest-energy state of the constituent filaments. Bundles containing these defects can minimize their elastic energy by taking on localized bends, which we call kinks. The presence of kinks allows one to relate the micron-scale contour of kinked filament bundles to their nanoscale structure, specifically, the presence of length-trapping defects. We show that the combination of theory and simulation of defected bundles can account for the distribution of kinks we observe in experiment. Over long times, defects slowly anneal in bundles. This slow relaxation of the bundle's structure can be understood in terms of the diffusion and interaction of the defects on it. Specifically, defects leave the bundle either through diffusion off the bundle's ends or by the annihilation of defects within it.

Not only do defected bundles explain the apparent kinks in collagen fibers, but the presence of defects also has implications for the collective elastic response of the bundle. In particular, we show that kinks are more bending compliant than undefected lengths of a bundle. As a result, we hypothesize that the collective mechanics of a network of defected bundles depends on the

Significance

A common structural motif for stress-bearing intracellular structures and tissues is a network of filament bundles. When observed in optical microscopy, these bundles often show localized bends—kinks—in their contour even though the stress-free state of their constituent filaments is straight. Using a combination of analytical mechanics and large-scale, finite-element Brownian dynamics simulations, we show that the optically observable kinks are related to topological defects in the interior, nanoscale structure of the bundle. Moreover, the kinks are more compliant to bending than the rest of the bundle. As a result, defected bundle networks must contain a random distribution of soft hinges, which, being the most compliant elastic elements, control the low-energy excitations of these bundle networks.

Author contributions: E.L.B., W.A.W., and A.J.L. designed research; V.M.S., M.J.G., and Q.H. performed research; V.M.S., M.J.G., Q.H., E.L.B., W.A.W., and A.J.L. contributed new reagents/analytic tools; V.M.S., M.J.G., Q.H., E.L.B., W.A.W., and A.J.L. analyzed data; V.M.S., M.J.G., Q.H., E.L.B., W.A.W., and A.J.L. wrote the paper; V.M.S. and A.J.L. provided the theory; M.J.G. and W.A.W. performed the simulations; and Q.H. and E.L.B. performed the experiment.

The authors declare no competing interest.

This article is a PNAS Direct Submission. Y.R. is a guest editor invited by the Editorial Board.

[1]To whom correspondence may be addressed. Email: valentinslepukhin@physics.ucla.edu.

This article contains supporting information online at https://www.pnas.org/lookup/suppl/doi:10.1073/pnas.2024362118/-/DCSupplemental.

Published April 5, 2021.

number and position of these quenched defects, which act like soft hinges in a 3D network of bundles that behave more like stiff beams.

Topological defects are well known in condensed matter, including, for example, disclinations in nematic liquid crystals and dislocations in crystalline solids (3–5). Defect motion plays a dominant role in the plastic deformation of many solids. Dislocations and disclinations are topological defects; their removal requires a system-sized reorganization of interatomic bonds. The defects in filament bundles share this feature. They cannot be removed without breaking a number of cross-links proportional to the bundle length (we consider the filaments to always be unbreakable). This feature ensures that the defects are long lived on the scale of the thermal undulations of the bundles themselves.

In our observations of collagen networks, we find kinked bundles, whose contour we quantify by measuring their local curvature using light microscopy. Due to their connection to the network, we cannot be certain that these kinks are not in some way related to elastic stress in the network. To address this question, we used large-scale Brownian dynamics simulations to study kinking in quenched filaments with force- and torque-free boundary conditions, finding that quenched defects produce a statistical distribution of kinks similar to those observed in the experiment. Using the simulations, we are also able to measure the reduction of the bundle's local bending modulus at the location of the defects and observe the motion of the defects along the bundle. Finally, we present theoretical calculations using a simple model of semiflexible filaments that demonstrate the relationship between defects and kinks in the bundle. Moreover, we analytically determine (and test via simulation) the time evolution of the number of defects in a bundle as they slowly anneal through defect–defect annihilation or by diffusion off the ends.

We first report our observations from light microscopy of kinks in collagen bundles and compare these kinks with those from numerical simulations. We then present a general discussion of the three types of defects and demonstrate that the minimum energy state of the defected bundle can be kinked. We explore defect dynamics, estimating the lifetime of a kink and the number of kinks in a bundle as a function of time, which we compare to simulation. To properly describe interaction of braiding type defects, we use the theory of the braid group; some relevant background is provided in *SI Appendix*, section 3.

Results

Experiment. The nanoscale structure of collagen is quite complex (6, 7). Small fibrils bind together to form larger fibrils, which, in turn, bind together to form fibers, which we observe in light microscopy. Given that these fibers associate rapidly and strongly with local bonds, collagen fibers are a good place to look for quenched defects in bundles and kinks, if such sharp bends of the bundle indeed result from those defects (8). In fact, kinked collagen bundles have been observed previously (9–11) using electron microscopy. These observations leave the possibility that the kinks observed in a single snapshot of a dynamic, flexible structure may be consistent with thermal undulations about a straight equilibrium state, rather than long-lived sharp bends (12). To address this question, we made multiple observations of collagen bundles in an aqueous environment to determine whether the time-averaged state of the bundles includes kinks.

We reconstituted pepsin-extracted type I bovine collagen and fluorescently labeled and imaged individual bundles. In Fig. 1*A*, we show 50 superimposed images of a single bundle (white on a black background) taken 0.5 s apart and showing three persistent kinks, which confirms that they are indeed long-lived structures. Green lines indicate the measurement of a kink angle. We measure the 2D projection onto the microscope's focal plane of the physical kink angle in three dimensions. We accept kink observations only when at least about 3 microns of bundle is observable on either side of the kink. In order for the image of the bundle to extend away from the kink on both sides, our reported kinks must lie in a plane making, at most, a small angle with respect to the focal plane. As a result, the discrepancy between our observed kink angle distribution and the physical one is quite small. We find less than 10% discrepancies between the projected and 3D, physical angle distribution when

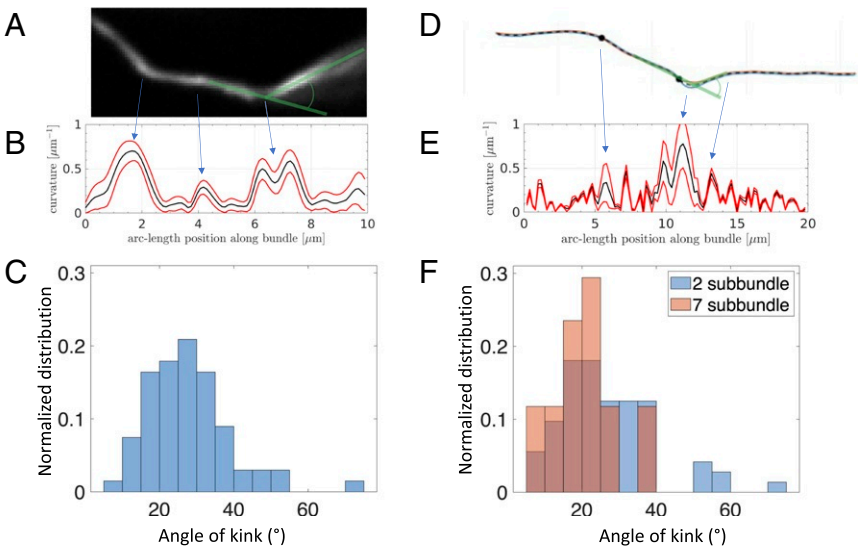

Fig. 1. Measurements of collagen bundles using fluorescence microscopy (*A*–*C*) and simulations (*D*–*F*). (*A*) Fluorescence image of a collagen bundle with noticeable kinks. Green traces show a measurement of the kink angle, given as angular deviation from straight. (*B*) Mean curvature (black) of a collagen bundle over 50 images. Red lines show the spread of curvature in time (1 SD). Blue arrows mark the locations of high curvature. (*C*) Histogram of mean kink angles for all measured bundles ($n = 74$). (*D*) A 2D simulation of bundles with reversible cross-linkers showing the bundle centerline (black dashed line), individual filaments (blue and red), and braids (black dots). (*E*) Mean of the curvature over 100 configurations (black). Red lines indicate 1 SD. (*F*) Kink angles from simulation for two-filament bundles in two dimensions and seven-filament bundles in three dimensions measured in the same way as in *C*.

testing this procedure with simulated data—see *SI Appendix*, section 1.

Seventy-four kink angle measurements from 43 bundles are summarized in Fig. 1*C*. The trace of the local curvature versus arc length along the bundle shown in Fig. 1*B* quantifies the points of high persistent curvature as indicated by the blue arrows. These local curvatures were computed by discretizing the contour using the intensity pixels in each image and computing the curvature from a cubic spline fit to these data. More details are given in *SI Appendix*, section 1. Repeating this procedure for other bundles, we observed kinks and determined their mean kink angles by averaging again over up to 50 repeated measurements of each kink angle. They showed temporal fluctuations with a nonzero mean. We present the distribution of kink angles for 74 kinks in Fig. 1*C*. There were larger variations between kink angles measured across multiple bundles than in the thermal fluctuations of a given kinked bundle. The distribution of these time-averaged kink angles has a mean at 26° and includes a range of typical angles between 7° and 55°. We observed one high-angle kink with a bend of 74°.

Many of the experimentally observed kinks appeared to be flexible. As a typical example, the kink angle of the bundle shown in *SI Appendix* , Fig. S1 had a mean of 29°, but fluctuated between 21° and 38°. Because the bundle's ends were constrained by the network, we cannot use these thermal fluctuations of the kink angle as a true measure of the kink's bending compliance.

Numerical Simulation. To better explore the nanoscale structure of the cross-section of the kinked bundles and to study the system with simpler, free boundary conditions, we turn to Brownian dynamics, finite-element simulations.

Our numerical model describes the semiflexible filaments as elastic objects via geometrically exact beam theory, and includes viscous dissipation (local drag), thermal forces, and the random binding and unbinding of cross-links (13–15). Bound cross-links are treated as short elastic beams making locally normal connections to the filaments to which they are bound. As a result, they act like so-called bundling cross-linkers that elastically constrain the angle between the bound filaments. Such linkers are well known in F-actin networks (16–18). The details of collagen intrabundle cross-linking are more poorly understood. In the absence of detailed models for these cross-linkers, we chose this simple linker model to promote bundling. Initially, all filaments were straight and parallel without any cross-links. To form bundles, a fixed concentration of cross-linkers was added to the finite-temperature (stochastic) simulation. The interaction of the thermally undulating filaments with transient cross-linkers leads to rapid bundle self-assembly (see *SI Appendix*, Fig. S4) with a number of quenched defects. Further details of the model and the setup of the computational experiments are provided in *Materials and Methods* and *SI Appendix*, section 2.

Observation and characterization of defects. A seven-filament bundle is shown in Fig. 2*A* from a simulation in three dimensions. Its contour deviates quite drastically from the trivial equilibrium shape of straight and parallel filaments, which are regularly cross-linked along their entire length. These metastable configurations of the bundle with localized bends—kinks—persist over long times as compared to the typical time scale of the angular fluctuations of the mean local tangent of the bundle. Over still longer times, the locations of the kinks move along the bundle, as described below. A movie of the bundle dynamics showing the shorter time scale bundle undulations can be found in Movie S1.

We observe two distinct classes of defects in the quenched bundles, which are all related to a mismatch between amount of filament arc length taken up per fixed unit length of the bundle. These are 1) braids, that is, rearrangements of filaments within the bundle, and 2) loops where one filament stores excess length by looping out of the bundle and then reattaching to it. Both braids (actually pseudo-braids, as described below) and loops are shown in Fig. 2*B* from a 2D simulation of two filaments where the filaments are allowed to cross each other but cannot untwist. This special setup is motivated by the fact that it is the smallest system capable of supporting a loop or a pseudo-braid. The pseudo-braid is a projection of a braid onto two dimensions and is the mechanical analog of a true braid in three dimensions. As will be shown in *Kinking Theory*, the energetics of the two-filament pseudo-braid is equivalent to that of a true 3D braid of three filaments when the two filaments making up the pseudo-braid have different bending moduli. The simplest system that supports true braiding defects is a three-filament bundle in three dimensions, shown in Fig. 2*C*. Fig. 2 *A*, *Inset* shows the typical structure of a loop in a larger bundle. There is also a third type of defect, 3) a dislocation in which a filament end appears within the bundle. This defect was not created in our simulations, due to the fact that we started the system with equal length filaments whose ends were initially aligned at one end of the simulation box. In the simulations, we concentrate on braids and loops. Defects observed in the 3D simulations were found to trap torsional as well as bending energy. The torsional torques measured in simulation were smaller than the bending torques that lead to kinking. We revisit this point in the discussion of our analytical model in *The model*. In the following sections, we first analyze the curvature of the bundle centerline as well as the kink angles resulting from braid and loop defects, and then investigate the dynamics of the defects, that is, how they move along the bundle and potentially interact with each other.

Curvature and kink angles of defected bundles. Fig. 1*D* shows a typical configuration of the minimal bundle setup with two filaments (blue and red) in two dimensions. The bundle centerline (black dashed line) is computed as the average of the two filament centerlines, and braids (black dots) are detected by the

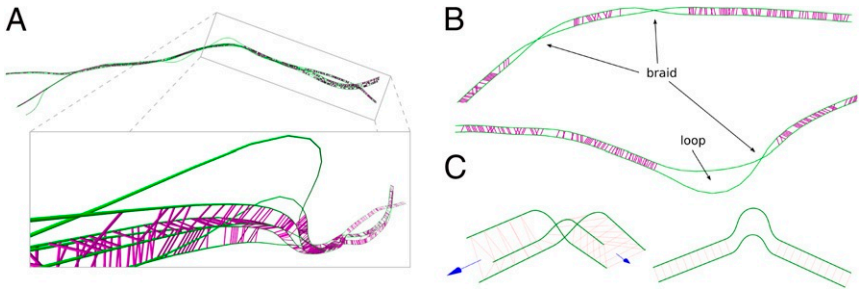

Fig. 2. Typical bundle shape and defects observed in numerical simulations of the bundle formation process, starting from initially straight and parallel filaments without any initial cross-links. (*A*) Example images show the entire bundle consisting of seven filaments (green) in three dimensions and approximately 1,600 cross-links (pink). (*Inset*) A magnified part. (*B*) Braids and loops observed in simulations with a minimal setup of two filaments (green) and transient cross-links (pink) in two dimensions. (*C*) Schematic of a braid (*Left*) and a loop (*Right*) as described in our analytical model.

crossings of the filament centerlines. A movie of the bundle's dynamics can be found in Movie S2. The curvature of the bundle's centerline as a function of centerline arc length is plotted in Fig. 1*E*, showing both the mean (black) and the standard deviation range (red lines) of the curvature computed from 100 simulation snapshots with a time interval of 1 s. Close to the midpoint of the bundle in the range of arc lengths $10\ \mu\text{m} < s < 12\ \mu\text{m}$, we observe two peaks in the curvature that are clearly visible as a double kink in the bundle configuration shown in Fig. 1*D*. These can be explained by the braid and loop defects there. The standard deviation of the curvature is increased by about one order of magnitude in this defected region, indicating a local increase in angular fluctuations at this point. This is a direct measure for the decreased effective bending modulus of the bundle in these defected, non–cross-linked regions. Using the relation between the thermal fluctuations of the local curvature and the bending modulus, we estimate a decrease in the effective bending modulus of about two orders of magnitude. Apart from the locally decreased bending modulus, such a defect most likely also leads to an anisotropy in the bundle's bending mechanics, which breaks another basic assumption of the ideal bundle as a single, thick filament. Similar features in the curvature data are observable for the second braid of this bundle at approximately $s = 6\ \mu\text{m}$ of this bundle. More examples are found in the other simulation runs. Additional results showing the curvature along the bundle at different time points are provided in *SI Appendix*, Fig. S5.

The histogram of measured kink angles over a total of 12 simulations is shown in Fig. 1*F*. Here, we applied the same procedure for the angle measurements as described for the experimentally obtained microscopy images in *SI Appendix*, section 1. The 3D simulation results were rotated such that the bundle centerline tangents left and right of the kink lie approximately within the image plane. The distribution of 72 kink angles for the two-filament bundle has a mean of 27°, with a standard deviation of 14° and values ranging from 4° to 77°. The kink angle distribution for larger bundles with seven filaments in three dimensions demonstrates a trend toward smaller angles and a more narrow distribution with 20±8° (mean ± standard deviation). Big bundles with up to 225 filaments will be investigated in more detail below.

Dynamics and interactions of defects. We now use our simulations to study dynamics on longer time scales, where we expect to see the motion of defects along the bundle and their annealing as the metastable, defected bundle slowly relaxes. To facilitate these observations, we need to speed up the motion of the defects by doubling the linker unbinding rate in our simulations to $k_{\text{off}} = 6\ \text{s}^{-1}$. At this rate, the motion of defects is still much slower than the undulatory fluctuations of the bundle, but now defect motion is moved into a time scale accessible by simulation, which covers 1,000 s.

Fig. 3 shows an example of how the (defected) configuration of a two-filament bundle evolves over time. We plot the position (measured by arc length) of braids (red dots) and cross-links (blue dots) along the bundle horizontally, with time increasing vertically. The resulting red tracks record the world lines of the braids over a simulated period of 500 s. The white vertical scars show cross-linker gaps in the otherwise densely cross-linked bundle. Due to a small offset between the filaments, there is a nearly persistent gap in cross-linking at the left end of the bundle where one filament stops. Cross-linkers appear in this gap because one filament slid far enough past the other to wrap around and briefly cross-link to the other one due to the periodic boundary conditions of the simulation box. We observe a pair of braids located near the bundle midpoint first emerge after ~ 20 s during the initial quench of the bundle. This time scale for the formation of the quenched bundle is typical and consistent with observation of the initial growth of the number of doubly bound cross-linkers; that number rapidly increases from zero at the beginning of a simulation and plateaus around 20 s, indicating the maturation of the defected bundle—see *SI Appendix*, Fig. S4 for further details on bundle self-assembly. Once the bundle has formed, the two braids in the middle approach each other and appear to annihilate, leaving a low cross-linker density region within the bundle during the time period of $100\ \text{s} < t < 270\ \text{s}$. After that time, a new pair of braid defects form. These slowly separate as more and more cross-links are formed between them.

The single braid close to the bundle's right end diffuses until it approaches the far right end of the bundle at $s \approx 19\ \mu\text{m}$ and at time $t \approx 280$ s. Here it vanishes by diffusing off the open end. The filaments simply uncross, and new cross-links are

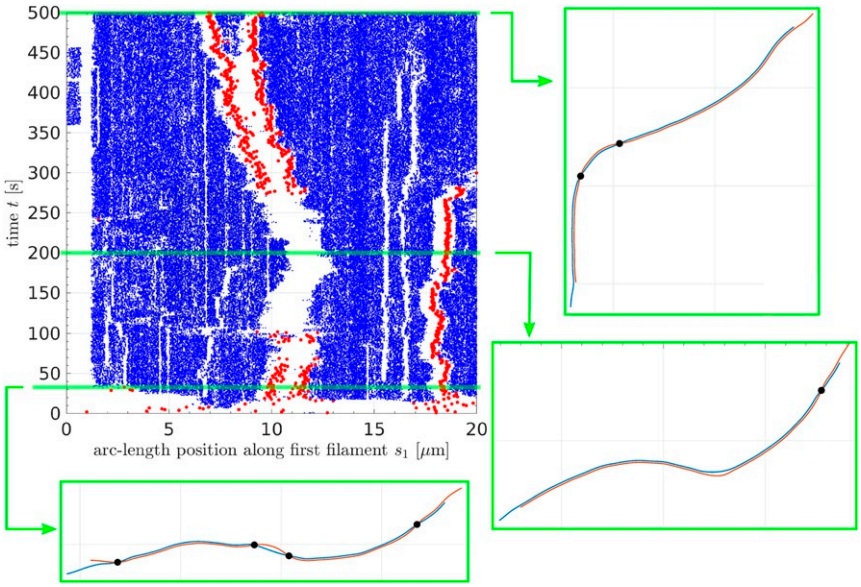

Fig. 3. Dynamics and interactions of defects observed in 2D numerical simulation. The position of braids (red dots) and cross-links (blue dots) along the (first, i.e., blue) filament is tracked over time. *Insets* (green frames) show the corresponding configuration of the two filaments (blue and red lines) and the braids (black dots) in the bundle at three different time points. See Movie S2 for an animation.

established between the unbraided filaments. Looking more carefully, one may observe a similar phenomenon on the left edge of the bundle. Immediately after the quench, there are actually four braids on the bundle, as indicated by the picture of the system at time slice $t = 34$ s. Almost immediately after this time and long before the next bundle configuration image at $t = 200$ s, that leftmost braid diffuses off the left end of the bundle. The final state of the bundle at $t = 500$ s shows a bent configuration where the localized bend near the center of the bundle is due to the two interacting braids that remain in the system. For these parameter values, the typical lifetime of a defect is hundreds of seconds.

Big bundles. Motivated by the fact that the number of filaments in a biopolymer bundle is likely to vary from $\mathcal{O}(1)$ to $\mathcal{O}(10^3)$, we explored simulations of very big bundles in three dimensions. Fig. 4*A* shows a self-assembled bundle with 225 filaments (white) and approximately 16,000 cross-links (pink). To rule out the influence of the initial arrangement of filaments in plane perpendicular to the bundle's mean tangent, we ran simulations with filament end points placed on a square grid in addition to the hexagonal grid. We observed no significant differences.

The large bundle's structure is hierarchical; one can identify more-tightly bound subbundles that form loops and braids with each other along the bundle's length. As observed already in 25-filament bundles, its centerline remains rather straight, while the subbundles show the characteristic kinks observed in the smaller bundles. One possible explanation for the rather straight form of the big bundles is their smaller aspect ratio as compared to the small bundles; in other words, very large bundles may well show kinks over longer distances, since such kinks require higher energy and are thus statistically less probable or more sparsely distributed defects. Simulations of big bundles with the same aspect ratio as the smaller ones remain computationally prohibitive. We observe, in the large bundle, a large hole created by a subbundle loop defect. Its appearance is strikingly similar to our experimental images of collagen bundles in Fig. 4*B*. Those parts of the images showing the hole defect are magnified and compared side by side in Fig. 4, *Insets*.

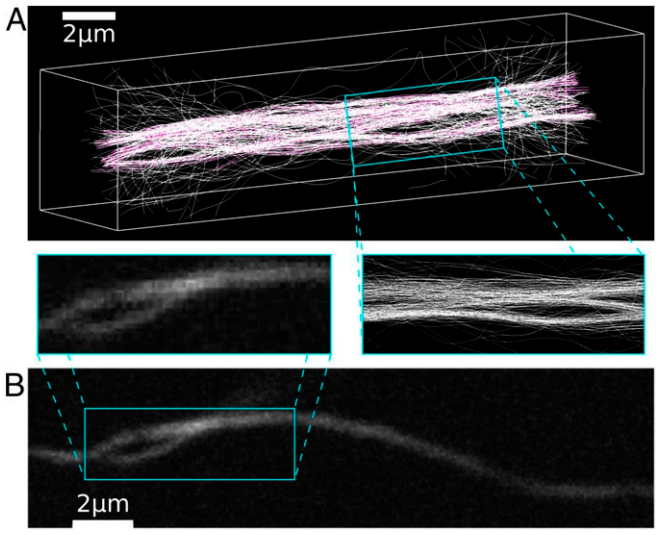

Fig. 4. Hole defect observed in simulation and experiment. (*A*) A 3D simulation of a big bundle with 225 filaments (white) and approximately 16,000 cross-links (pink). (*B*) Fluorescent confocal laser scanning image of a collagen bundle. Those parts of both images showing the hole defect are magnified and compared side by side in *Insets*.

Kinking Theory.

The model. We now examine the energetics of kink formation using a simple model consisting of a bundle of n inextensible, semiflexible filaments connected by cross-links. The filaments' elasticity is controlled by a single bending modulus κ. The filaments are arranged so that their mean tangent directions are parallel along the $\hat{x}$ axis. In a cross-section normal to this direction (the yz plane), the filaments' centers lie on a triangular lattice with a lattice constant equal to the size of the cross-linkers. The cross-linkers are assumed to locally constrain both the distance between the cross-linked filaments and their crossing angle, so that the cross-links are normal to the filaments to which they bind. We further assume that the cross-linking is reversible; that is, they bind and unbind from the filament bundle so that the cross-linker density within the bundle remains in chemical equilibrium with a solution of free cross-linkers at a fixed chemical potential. Previous work has shown that thermal undulations of the filaments induce Casimir forces between cross-links (19, 20) and cause the transition between states of free filaments and a densely cross-linked bundle to be a discontinuous or first-order phase transition rather than a smooth crossover. Here we work at chemical potentials above this transition so that we may assume dense cross-linker coverage; hereafter, we neglect Casimir interactions and other fluctuation-induced effects.

If all the bundle's filaments have the same length, the energetic ground state is a straight bundle with as many cross-links as possible. However, if at least one of the filament's length differs from those of others, the straight bundle configuration will necessarily have a defect where a filament's end occurs within the bundle. That dislocation defect may, in fact, be unstable toward forming a kink in the bundle's interior, leading to a kink in the elastic ground state of the system (we explore this point in *Dislocations*).

When we consider metastable states, there are many more options. If removing a defect in the structure of cross-linked straight filaments requires uncoupling a large number of cross-links, the lifetime of that defect may exceed the time of the experiment. We divide such defects into two groups: defects due to the deviation of the filament from its straight state (loop) and the effects due to the permutations of the filaments (braiding). We study the simplest cases of these effects in *Loops* and *Braids*, respectively.

In all these cases, the energy of the bundle can be written as the sum of two terms: the bending energies of the n constituent filaments and the energy of their chemical interactions with the cross-links,

$$E = \sum_{i=1}^{n} \int ds \left\{ \frac{\kappa_i}{2} \left(\partial_s \hat{t}_i\right)^2 + \mu \right\}, \qquad [1]$$

where $\hat{t}_i$ is unit tangent vector of filament i. The integral is taken over the piece of the filament ℓ without cross-links, which generates the term $\mu\ell$ equal to the work of unbinding the cross-links in this piece, where μ is a linker binding energy per unit length. Eq. **1** implicitly assumes a linear elastic response of the material to bending deformation in that the bending torque is proportional to the bending angle. The parameterization of local curvature, however, is exact, even for large bending. In essence, we use the usual assumption (21) that, due to the thinness of the filaments, there are no large strains within the filament cross-section even at large curvatures, so constitutive bending nonlinearities may be neglected even for highly deformed filaments.

Since we assume that the cross-links completely fix both angle and positions of the filaments, the piece of the filament with cross-links is straight and parallel to the whole bundle. We now minimize the bundle's energy subject to boundary conditions that enforce the presence of one or more defects. If a kinked configuration minimizes this energy, we conclude that elasticity

theory predicts a kink. This calculation will also determine the optimal size (length) and bending angle of the kink, which we report below. All such calculations assume that the defects do not trap filament torsion. We note, from simulation, that typical defects include some torsional deformations. As a result, our calculations represent the minimum energy configurations of each defect. We anticipate there to be a continuous spectrum of excited defect states associated with increasing torsional energy. We now perform this minimization for the three different types of defects.

Loops. We start with the simplest case of a two-filament bundle, forming a loop defect by demanding that the filaments have disparate lengths $L_1 \neq L_2$ between consecutive cross-links. What results is the bending of the whole bundle to form a kink (Fig. 2*B*). This approach generalizes to n-filament bundles, and can be adapted to large bundles in which two subbundles form a loop. To simplify this calculation, we take the size of the cross-links and the filaments' diameter (whose sum is a) to be zero. In case of loops, the excess trapped length in the defect is not principally controlled by that length, so, in this case, the $a = 0$ limit both is reasonable and simplifies the calculation. Then the boundary conditions for the position of the ends of the filament are integral conditions on the tangent vector,

$$\int_{-L_1/2}^{L_1/2} ds\hat{t}_1(s) = \int_{-L_2/2}^{L_2/2} ds\hat{t}_2(s), \qquad [2]$$

and boundary conditions for the tangent vector determine the kink angle ϕ, which is the total bend of the tangent across the structure. We pick a reference frame so that these boundary conditions are symmetric,

$$\hat{t}_1(\pm L_1) = \hat{t}_2(\pm L_2) = \begin{pmatrix} \cos(\phi/2) \\ \sin(\phi/2) \end{pmatrix}. \qquad [3]$$

Minimizing the energy from Eq. **1** in the limit of small filament bending ($\hat{t}_y \ll 1$), we obtain a lengthy self-consistent equation for the angle ϕ (see *SI Appendix*, section 3), which can be simplified in the case of the equal bending moduli $\kappa_1 = \kappa_2 = \kappa$ to

$$\phi = \gamma \left(\Delta L \sqrt{\frac{\mu}{\kappa}} \right)^{1/3}, \qquad [4]$$

with the numerical constant $\gamma \approx 0.93$, and $\Delta L = L_2 - L_1 \neq 0$. We verified these results by minimizing the energy numerically (Fig. 6*A*). Loops produce a continuous spectrum of kink angles that grow as the cube root of their length mismatch. As expected, an increase in the bending modulus suppresses this kink angle, while an increase in the linker binding energy increases it by shrinking the extent of the gap in the cross-linking. We now turn to braids.

Braids. The simplest model of braiding in three dimensions requires three filaments. Braiding of two filaments in three dimensions can be undone by twisting the bundle about its long axis; it is not topologically protected (the relationship between braiding and rotation is discussed in more detail in *SI Appendix*, section 3). The minimum energy configuration of three cross-linked filaments with the same length will be a right prism with an equilateral triangle as its base. We choose a coordinate system so that the x axis lies parallel to the filaments, filaments 2 and 3 are in the xz plane, and filament 1 is above that plane. To introduce a braid, we require filament 1 to go from above to below the xz plane (Fig. 2*C*). This configuration is metastable, since we need to decouple all the cross-links on one side to get to the minimal energy configuration. There is no rotation of an end of the bundle that will eliminate the braid.

Since the cross-links fix both relative angle and position of the filaments, filament 1 cannot be connected to filaments 2 and 3 by the cross-links in the defect core; however, filaments 2 and 3 can remain cross-linked. Thus, filaments 2 and 3 behave as one combined filament 2′ with double the bending stiffness, and remain in the xy plane like filament 1. As a result, a true three-filament braid in three dimensions is energetically equivalent to a two-filament pseudo-braid, as introduced in our simulations.

The boundary conditions on the vector $\hat{t}$ are the same as in the previous case, Eq. **3**, but the displacement boundary condition differs, incorporating the finite filament radius and cross-linker length a, which is necessary for the braid to trap excess length. We find

$$\int_{-L_1/2}^{L_1/2} ds\hat{t}_1(s) = \int_{-L_2/2}^{L_2/2} ds\hat{t}_2(s) + 2a\cos(\phi/2)\hat{y}. \qquad [5]$$

Unlike in looping, we do not fix the filament length mismatch $\Delta L = L_2 - L_1$, but instead allow it to vary to relax the braid's energy. It is conceivable that one may encounter higher-energy braids in which braiding and an excess of trapped length (looping) coexist. We do not study this case here.

We observe that braids should generate local bending, at least in the limit of a sufficiently soft bending modulus. The binding free energy (chemical potential difference between free and bound linkers) acts as an effective tension on the bundle. Setting the bending modulus to zero and fixing the length of the braided region, the solution for the filament contours inside the braid will be straight lines. In this configuration, linker-induced tension generates a torque that increases the kink angle of kinked configurations (Fig. 5*A*). To stabilize this angle at a finite value, we must include finite bending compliance. We do so now, turning to the full calculation.

Calculating the energy of the braid as a function of the kink angle ϕ, we find that kinking is controlled by the dimensionless parameter

$$\zeta_i = \frac{\mu a^2}{\kappa_i}, \qquad [6]$$

where μ is the cross-linker binding energy per unit length, κ_i is the bending modulus of filaments of type i, and the length a is the normal distance between the centerlines of a pair of

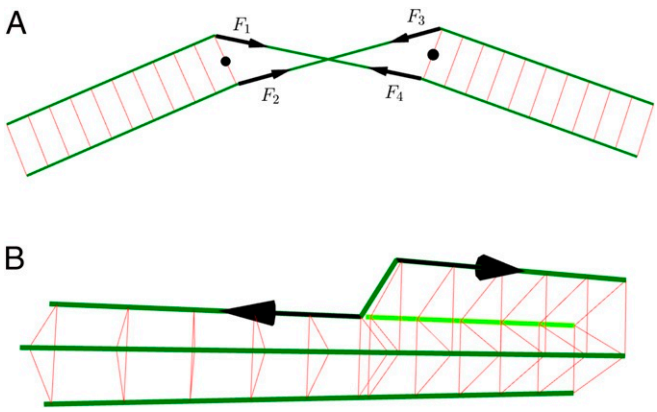

Fig. 5. (*A*) Braid in the limit of zero bending. Forces F_1, F_2, F_3, F_4 (black arrows) have equal magnitude, but F_2 and F_4 create a larger torque (relative to the middle of the corresponding cross-link; black dots). This torque leads to the rotation of the left piece of the bundle counterclockwise and of the right piece clockwise, that is, it increases the angle of the kink. (*B*) Dislocation in the limit of zero bending. The least-energy configuration is a straight bundle, with one filament rearranging at the right angle when filament 4 (chartreuse) stops, immediately taking its place. However, if we increase the bending to nonzero, this segment under the right angle tries to straighten, producing repulsive forces (black arrows). These forces create an uncompensated torque at the left and right parts of the bundle, leading to a kink.

bound filaments. This length can be interpreted to be the sum of the radii of the filaments and the length of the cross-linking molecule. ζ is the ratio of the linker binding energy per unit length μ to an energy per length set by bending on the scale of the interfilament separation, κ/a^2. In general, we expect larger ζ values to lead to kinking. Below, we verify this intuition. Larger values of the linker binding energy and interfilament separation increase filament bending in the defected region. This bending, which is opposed by κ, provides the torques necessary to produce the kinks. The nonphysical limit of zero interfilament distance ($a \to 0$) implies that braids involve no filament bending and thus generate no bending moments necessary for kinking.

We prove, in *SI Appendix*, section 3, that, for small values of ζ_i, the energy is minimized at $\phi = 0$; that is, there are no kinks. For large values of ζ_i, the minimum energy states are kinked ($\phi > 0$). We examine this transition in more detail for the case $\kappa_1 = \kappa_2$. We assume symmetric bending, $\alpha_1(s) = -\alpha_2(-s)$, noting that numerical solutions of the minimization show that the symmetric solution based on this ansatz indeed identifies the global energy minimum. We obtain (see *SI Appendix*, section 3)

$$\lambda^2 \sin^2(\phi/2) = \frac{8\kappa^2}{a^4}(\zeta - 2), \qquad [7]$$

where we introduced a Lagrange multiplier λ to enforce the $\hat{y}$ component of Eq. **5**, which plays the role of the tensile force in $\hat{y}$ direction. When ζ increases to two, there is a second-order transition at which the kink angle grows continuously from zero as ζ increases. Near the critical point $\zeta = 2 + \epsilon$, $\phi \approx \sqrt{\epsilon}$. Numerical minimization of the energy from Eq. **1** leads to the same result (Fig. 6*B*). In that figure, we also see (red dots) that, when the two filaments have differing bending moduli, there is a first-order kinking transition where the kink's angle jumps discontinuously from zero at the critical value of ζ.

Dislocations. The simplest dislocation requires a bundle of four filaments in three dimensions where one of the four ends within the bundle. The stable state of four filaments is a right prism formed by a base of two equilateral triangles sharing one edge, as shown in Fig. 5*B*. We label these triangles as 1-2-4 and 2-4-3; only filaments 1 and 3 are not cross-linked to each other. If either filament 1 or 3 ends within the bundle, the configuration remains stable because the other three form a stable three-filament prism. But, if another filament ends, for example, filament 4, the remaining filaments must deform to recreate a cross-section with an equilateral triangle (Fig. 5*B*). Due to cross-linker constraints, the distortion associated with the defect must locally remove cross-linkers between two of the filaments. Without loss of generality, we demand that filaments 2 and 3 remain cross-linked. Calculating the energy associated with this defect is complicated by the fact that there is no mapping to a 2D version of the distortion. To gain immediate insight, it is helpful to consider, momentarily, the unphysical case of zero filament bending modulus. Then filaments 2 and 3 remain straight, but filament 1 makes two right-angle bends at the defect to move to the location of the missing filament 4 and thereby maximize cross-linking. If we now reintroduce a finite bending modulus, this localized dislocation will spread out along the bundle to decrease bending energy at the expense of reducing the maximal cross-linking shown in Fig. 5*B*. A force pair is also introduced by filament 1's bending (shown in the figure as black arrows) which produces a torque causing the entire bundle to kink. We perform numerical minimization of the energy assuming that filaments 2 and 3, being cross-linked everywhere, form a ribbon that can bend in the direction perpendicular to its plane with bending modulus $\kappa_{\text{ribbon}} = 2\kappa$, but is absolutely rigid in the direction parallel to its plane. The results of our qualitative analysis above are consistent with the quantitative energy minimization (Fig. 6*C*)—the maximum of the kink angle is observed to be at a finite value of ζ. Zero and infinite values of that parameter lead to a zero kink angle.

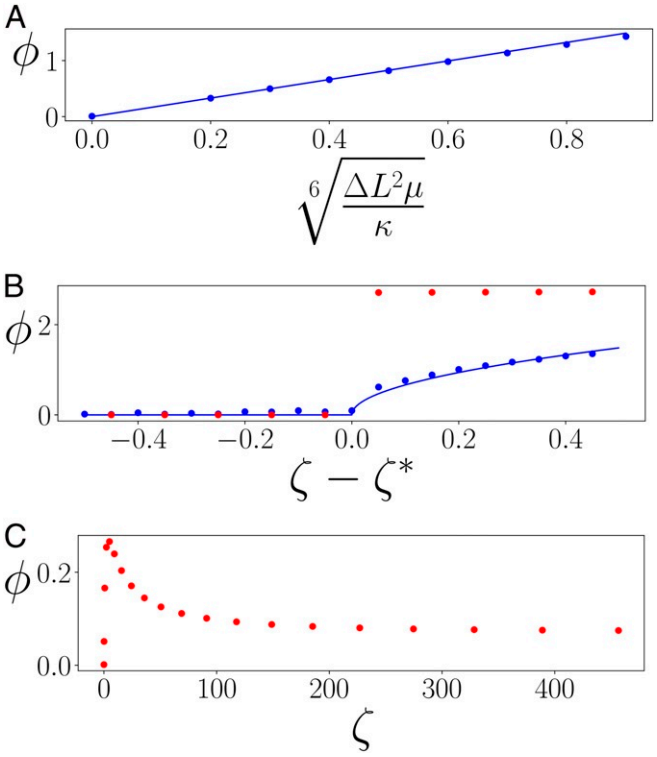

Fig. 6. Kink angle ϕ as a function of a dimensionless parameter for (*A*) loops, (*B*) braids, and (*C*) dislocations showing both numerical solutions to the energy minimization (circles), and the analytic predication (solid line). We show two cases, $\kappa_1 = \kappa_2$ (blue) and $\kappa_1 = 2\kappa_2$ (red). (*A*) Numerical results agree with the small angle theoretical prediction even up to $\phi \approx \pi/2$. (*B*) For the symmetric case $\kappa_1 = \kappa_2$, the angle ϕ produced by the braid grows as $\sqrt{\zeta - \zeta^*}$ with $\zeta^* = 2$. The coefficient of proportionality for the analytical curve was chosen to best fit the data. For the asymmetric case, there is a discontinuous (first order) jump in ϕ at $\zeta^* \approx 12.25$. (*C*) For dislocations, the angle reaches a maximum at a finite value of ζ and goes to zero at $\zeta = 0$ and $\zeta = \infty$.

Defect Dynamics. Over times significantly longer than those associated with the undulations of the bundle, defects can move along the bundle and interact. These dynamics require multiple cross-linker binding/unbinding events. As a result of these events, defects move diffusively and may eventually fall off the ends of the bundle. In the case of dislocations and braids, defects may combine or annihilate. For the latter type, these interactions are controlled by the structure of the braid group.

Consider two braids—a braid/antibraid pair—separated by N cross-links. Since these defects would annihilate if the intervening cross-links were removed, we may expect this pair might vanish if their separation becomes sufficiently small. The braids are motile, with a diffusion constant set by the linker detachment rate k_{off}, and do not strongly interact when separated by lengths greater than the defect core size. The probability density $p(n, t)$ of there being n cross-links separating the two defects at t then obeys a diffusion equation,

$$\frac{\partial p(n,t)}{\partial t} = 2k_{\text{off}} \frac{\partial^2 p(n,t)}{\partial n^2}. \qquad [8]$$

Using a well-known result for the first mean passage time (22), the mean lifetime of this braid/antibraid pair is

$$T = \frac{3\,N^2}{k_{\text{off}}}. \qquad [9]$$

For the simulations presented in Fig. 3, we have $k_{\text{off}} = 6\,\text{s}^{-1}$, $N \approx 15$ to 35. Then Eq. **9** predicts $T \approx 100$ to 500 s, while, in Fig. 3, we obtain $T \approx 200$ s, within the predicted range.

For a three-filament bundle, the dynamics of N braids is equivalent to the diffusion of N particles (braids) of three types, which are randomly distributed after a quench. The braid group (see *SI Appendix*, section 3) requires that a particle of one type can annihilate only with particles of one other type. If particles encounter each other and cannot annihilate, we assume they stick, since, by merging their defected regions, the net number of cross-linkers on the bundle increases. Using these dynamical rules, we studied the annealing of braided bundles using Monte Carlo simulations—results are shown in *SI Appendix*, section 3.

Simple combinatorics shows that annihilation events are less common than braid combination (sticking), since the former requires braid/antibraid adjacency. Since the number of different braid group operators grows linearly with the number of filaments in the bundle, the probability for braid/antibraid adjacency decreases with increasing braid size. When considering large bundles, we can neglect annihilation. Doing so and using a mean-field approximation, we let $\rho(x, t)$ be the braid density, implying that the average distance between neighboring braids is $1/\rho$. The time to halve the number of braids will then be $t_{1/2} \propto 1/\rho^2 k_{\text{off}}$ according to Eq. **9**. The same logic implies that the continuous rate of decrease of the braid density will obey

$$\frac{d\rho}{dt} = -\alpha\rho^3, \qquad [10]$$

where α is a phenomenological parameter accounting for the probability of braids combining upon close approach. Solving Eq. **10**, we find $\rho \propto t^{-1/2}$, which is a general result for sticky (or annihilating) random walkers (23). The predictions of this mean-field model are consistent with our Monte Carlo simulations and with the Brownian dynamics simulations of the full bundle model—see *SI Appendix*, Fig. S6.

We briefly mention the dynamics of loop and dislocation defects. Complete annihilation of loop defects is highly unlikely, as it would require the amount of trapped length in the two loops to match. We expect loop defects to diffuse along the bundle and, in larger bundles, to pass through each other. Dislocations should also diffuse by a type of repetitive motion (as in polymer melts) in which the filament end detaches within the bundle, forms a loop, and reattaches. Thus, dislocations in an otherwise ordered bundle should retract toward the bundle edge with more filaments in it. After loops are formed, the dislocation should perform a biased random walk, due to the fact that the energy of loop defects will suppress further retractions of the dislocation core toward the bundle's end.

Discussion

Biopolymer filament bundles are kinked despite the fact that the elastic ground state of their constituent filaments is straight, as clearly seen in our experiments on collagen bundles. In this article, we quantified these kinks and proposed that their existence can be attributed to defects quenched into the bundles during cross-linking. These defects come in three classes: loops, braids, and dislocations. This proposal is supported both by analytic calculations of the energy-minimizing contour of bundles containing these defects and by finite-element Brownian dynamics simulations of the quenched bundles of 2 to 200 filaments. The mechanical connection between these defects and kinks (high-curvature regions) of the bundle is straightforward—defects generate a local distortion of the filaments driven by cross-linking. The entire bundle may bend, producing a kink in order to compensate for that distortion. This mechanism is reminiscent of the relaxation of a flexible hexatic membrane in the vicinity of a disclination (24). There, a topological defect relaxes local strain via a puckering of the membrane that produces long-ranged Gaussian curvature. Here the distortion of the bundle may be entirely localized in a sharp bend.

In our experiments, we found that 4% of the observed collagen bundles had one or more kinks and that these kink angles had a mean of 26°, but were quite varied, ranging up to 74° in the sample of 74 kinks studied. When we consider that loop defects can produce a continuous distribution of kink angles, it seems natural to suppose that this defect is the predominant cause of kinking. The number of observed kinks is likely an underestimate of the real system, due to the limitations of our imaging that shows only those bundles lying in the imaging plane. Only kinks oriented so that the bundle bends within the imaging plane are observable.

The kinks associated with both braids and dislocations are expected to be narrowly distributed at angles set by the number of filaments in the bundle, since these defects produce fixed kink angles that depend only on that number, the cross-linker binding energy, and bending moduli of the filaments. For a fixed number of filaments, both dislocations and braids produce kink angles that depend on only a single dimensionless number $\zeta = \mu a^2/\kappa$. In the case of braids, the kink angle grows from zero at a critical value of ζ, which depends on the number of filaments but is roughly of order unity. Looking at stiff F-actin cross-linkers like α-actinin, we find that $\zeta \approx 0.1$; it is too small for braids to generate kinks. We do, however, expect braids to be associated with kinks in softer filament systems such as DNA condensed by polyvalent counter ions (25, 26) or cross-linked intermediate filaments (27, 28) where $\zeta \approx 10$ to 100. Currently, our understanding of collagen bundle cross-linking is less precise; our estimate in this system is that $\zeta \approx 0.1$ (see *SI Appendix*, section 1). This suggests that loops certainly should produce kinks and that braids should not. However, given the large uncertainty in our estimate of ζ, it is conceivable that braids are also kink-generating defects. Of course, even if braids do not produce kinks, we expect them to be present and to produce high-flexibility "hinges" in the bundle. Dislocations always generate kinks, but the kink angle is appreciable only when $\zeta \approx 1$. We surmise (with the same caveats regarding the uncertainty of ζ) that dislocations are unlikely to be responsible for the experimentally observed kinks in the collagen bundles.

Another argument for loop-controlled defects in collagen is a presence of z-shaped double kinks (see *SI Appendix*, Fig. S7 for the examples), which can be attributed to slippage between two filaments in a bundle such that they produce a pair of loops. The lengths stored in this pair are such that, after the two loops, the filaments once again have no length mismatch.

The lifetime of these defects appears to be significantly larger than the characteristic time of thermal undulations of the filaments and longer than the typical observation time in experiment. This is supported by the experimental data, where kink annihilation or diffusion to the ends is never observed. When we study kink dynamics via simulation on the time scales significantly longer than those covered by experiment, we observe their diffusion, sticking, and annihilation, which one expects from the theory. Specifically for braids, we find that their motion is consistent with particles diffusing in one dimension, with interactions obeying the rules of the braid group. We speculate that bundles under compression may relieve stress by the pair production of braid/antibraid pairs in a manner resembling the Schwinger effect (29, 30).

Examining Fig. 4 leads us to speculate that very large bundles of many filaments might be considered to be smaller bundles composed of more weakly bound subbundles, which are themselves composed of the original filaments. If we may consider

this hierarchical approach, we can replace a in ζ by the subbundle radius and write the bending modulus in terms of that radius as well, using $\kappa \approx Ea^4$, where E is the Young's modulus of the material (typically in the 1 GPa range for proteins). In that case, we see that $\zeta \approx (\mu/E)a^{-2}$, so that, as the radius of the subbundles increases, ζ decreases rapidly. As a result, we expect that kinks in larger bundles will be dominated by loop defects regardless of the value of ζ for the original filament system.

When considering very large bundles, one may ask whether cross-linkers deep in the bundle's interior remain in equilibrium with the cross-linker concentration in the surrounding fluid. Due to steric hindrance, these internal linkers may diffuse slowly out of the bundle, leading to a linker chemical potential gradient across the bundle's radius on measurable time scales. We do not incorporate such effects in our simulations, and we do not expect them to be relevant in the case of our collagen bundles where we do not have exogenous linkers. But this nonequilibrium effect, where relevant, may introduce intriguing viscoelastic effects in the bending dynamics of very large bundles.

Many biopolymer filaments are chiral, and their chirality is known to affect their packing into tight bundles (31–33). In particular, chirality introduces a form of geometric frustration in these tightly packed bundles. We suspect that the defects discussed here may play a role in reducing the elastic stress-associated chirality-induced packing frustration, and thus may be important for understanding the long length-scale structure of such chiral bundles.

We note that defects rather generally produce weak links in the bundle where, due to the absence of cross-linking, the effective bending modulus of the bundle is reduced by at least an order of magnitude. This suggests that the collective mechanics of a rapidly quenched bundle network might be dominated by these defects, which introduce a set of soft joints into the otherwise quite stiff bundles. As a result, rapidly quenched bundle networks may be anomalously compliant as compared to their annealed state. It is interesting to note that these defects provide soft hinges in the network (rather than universal joints) and that there may well be many more such soft hinges than there are kinks, since not all defects generate kinks, but all disrupt the local cross-linking. Currently, there are no kinetic theories of bundling that allow us to estimate the number of such soft hinges in a network of filament bundles and then attempt to predict the mechanics of the defected network. Of course, filament bundle networks produced by transient cross-linkers have a complex rheological spectrum, including a low-frequency power law regime (34, 35). Understanding the mechanical effect of these soft hinges on that low-frequency rheology remains an interesting direction for future studies.

Materials and Methods

Experiments. Type I bovine pepsin extracted collagen (PureCol 5005-100 ML lot 7503, Advanced BioMatrix) was reconstituted according to Doyle (36). Reconstituted collagen solution was diluted to 0.2 mg/mL with phosphate-buffered saline and was incubated at 37 °C overnight. The collagen was fluorescently labeled (Atto 488 NHS ester 41698-1MG-F lot BCBW8038, Sigma-Aldrich) and then imaged with Olympus Fluoview1200 laser scanning confocal microscope using a 60×1.45NA oil immersion objective. To construct a trace of the bundle, Matlab was used to determine the position of bundle in each row of the image defined as the mean of the Gaussian fit of the pixel intensity across each row. A cubic spline is used to estimate the curvature along the bundle. The kink angles were measured using imageJ. Further details can be found in *SI Appendix*, section 1.

Simulations. In our numerical model, the individual semiflexible filaments are described via nonlinear, geometrically exact, 3D Simo–Reissner beam theory (37, 38) and discretized in space by suitable finite element formulations (39, 40). Their Brownian dynamics is modeled by including random thermal forces and viscous drag forces along the filament (13, 14). We apply an implicit Euler scheme to discretize in time, which allows us to use relatively large time step sizes (13, 14). Cross-links are modeled as additional, short beam elements between distinct binding sites on two filaments, which bind and unbind randomly based on given reaction rates and binding criteria (15). In particular, the latter include a preferred distance between binding sites and a preferred angle between filament axes that need to be met such that a linker molecule switches from the free to the singly bound state or from the singly to the doubly bound state. Altogether, this finite element Brownian dynamics model turns out to be a highly efficient numerical framework, which enables large-scale simulations with hundreds of filaments over hundreds of seconds and has been used in several previous studies (15, 20, 35, 41–43). We used the existing C++ implementation in our in-house research code BACI (44), which is a parallel, multiphysics software framework. In addition, we used self-written Matlab (45) scripts for the data analysis and used Paraview (46) for the visualization of the system. Further details about the numerical model, including all parameter values and the detailed setup of the computational experiments, can be found in *SI Appendix*, section 2.

Data Availability. Raw images and simulation results can be found on Dryad (47).

ACKNOWLEDGMENTS. A.J.L. and V.M.S. acknowledge partial support from Grant NSF-DMR-1709785. V.M.S. acknowledges support from the Peccei scholarship and the Bhaumik Institute Graduate Fellowship. W.A.W. and M.J.G. acknowledge partial support from Bavaria California Technology Center. E.L.B. and Q.H. acknowledge support from the US Air Force Office of Scientific Research FA9550-17-1-0193 and the Office of the President of the University of California.

1. M. Bathe, C. Heussinger, M. Claessens, A. Bausch, E. Frey. Cytoskeletal bundle bending, buckling, and stretching behavior. arXiv [Preprint] (2006). https://arxiv.org/abs/q-bio/0607040v2 (Accessed 31 March 2021).
2. C. Heussinger, M. Bathe, E. Frey, Statistical mechanics of semiflexible bundles of wormlike polymer chains. *Phys. Rev. Lett.* **99**, 048101 (Jul 2007).
3. P. M. Chaikin, T. C. Lubensky, *Principles of Condensed Matter Physics* (Cambridge University Press, 1995).
4. M. Kleman, *The Topological Classification of Defects* (Springer US, Boston, MA, 1995).
5. D. R. Nelson, *Defects and Geometry in Condensed Matter Physics* (Cambridge University Press, 2002).
6. M. D. Shoulders, R. T. Raines, Collagen structure and stability. *Annu. Rev. Biochem.* **78**, 929–958 (2009).
7. M. J. Buehler, Nature designs tough collagen: Explaining the nanostructure of collagen fibrils. *Proc. Natl. Acad. Sci. U.S.A.* **103**, 12285–12290 (2006).
8. P. Kannus, Structure of the tendon connective tissue. *Scand. J. Med. Sci. Sports* **10**, 312–320 (2000).
9. M. Franchi, V. Ottani, R. Stagni, A. Ruggeri, Tendon and ligament fibrillar crimps give rise to left-handed helices of collagen fibrils in both planar and helical crimps. *J. Anat.* **216**, 301–309 (2010).
10. S. P. Reese, N. Farhang, R. Poulson, G. Parkman, J. A. Weiss, Nanoscale imaging of collagen gels with focused ion beam milling and scanning electron microscopy. *Biophys. J.* **111**, 1797–1804 (2016).
11. T. Gutsmann *et al.*, Evidence that collagen fibrils in tendons are inhomogeneously structured in a tubelike manner. *Biophys. J.* **84**, 2593–2598 (2003).
12. Y. Wakuda, S. Nishimoto, S.-I. Suye, S. Fujita, Native collagen hydrogel nanofibres with anisotropic structure using core-shell electrospinning. *Sci. Rep.* **8**, 6248 (2018).
13. C. J. Cyron, W. A. Wall, Consistent finite-element approach to Brownian polymer dynamics with anisotropic friction. *Phys. Rev.* **82**, 66705 (2010).
14. C. J. Cyron, W. A. Wall, Numerical method for the simulation of the brownian dynamics of rod-like microstructures with three-dimensional nonlinear beam elements. *Int. J. Numer. Methods Eng.* **90**, 955–987 (2012).
15. K. W. Müller, C. Meier, W. A. Wall, Resolution of sub-element length scales in Brownian dynamics simulations of biopolymer networks with geometrically exact beam finite elements. *J. Comput. Phys.* **303**, 185–202 (2015).
16. P. Matsudaira, Actin crosslinking proteins at the leading edge. *Semin. Cell Biol.* **5**, 165–174 (1994).
17. S. J. Winder, K. R. Ayscough, Actin-binding proteins. *J. Cell Sci.* **118**, 651–654 (2005).
18. T. D. Pollard, Actin and actin-binding proteins. *Cold Spring Harb. Perspect. Biol.* **8**, a018226 (2016).
19. D. Kachan, R. Bruinsma, A. J. Levine, Casimir interactions in semiflexible polymers. *Phys. Rev. E* **87**, 032719 (2013).
20. D. Kachan, K. W. Müller, W. A. Wall, A. J. Levine, Discontinuous bundling transition in semiflexible polymer networks induced by casimir interactions. *Phys. Rev. E* **94**, 032505 (2016).
21. L. D. Landau, E. M. Lifshitz, *Theory of Elasticity* (Oxford University Press, ed. 2, 1986).
22. N. G. Van Kampen, *Stochastic Processes in Physics and Chemistry* (North Holland, 2007).
23. J. Cardy, U. C. Täuber, Theory of branching and annihilating random walks. *Phys. Rev. Lett.* **77**, 4780–4783 (1996).

24. J.-M. Park, T. C. Lubensky, Topological defects on fluctuating surfaces: General properties and the Kosterlitz-Thouless transition. *Phys. Rev.* **53**, 2648–2664 (1996).
25. G. S. Manning, The persistence length of DNA is reached from the persistence length of its null isomer through an internal electrostatic stretching force. *Biophys. J.* **91**, 3607–3616 (2006).
26. E. Raspaud, M. Olvera de la Cruz, J.-L. Sikorav, F. Livolant, Precipitation of DNA by polyamines: A polyelectrolyte behavior. *Biophys. J.* **74**, 381–393 (1998).
27. E. E. Charrier, P. A. Janmey, Mechanical properties of intermediate filament proteins. *Methods Enzymol.* **568**, 35–57 (2016).
28. E. Haimov, R. Windoffer, R. E. Leube, M. Urbakh, M. M. Kozlov, Model for bundling of keratin intermediate filaments. *Biophys. J.* **119**, 65–74 (2020).
29. J. Schwinger, On gauge invariance and vacuum polarization. *Phys. Rev.* **82**, 664 (1951).
30. J. Schwinger, The theory of quantized fields. 5. *Phys. Rev.* **93**, 615–628 (1954).
31. G. M. Grason, R. F. Bruinsma, Chirality and equilibrium biopolymer bundles. *Phys. Rev. Lett.* **99**, 098101 (2007).
32. G. M. Grason, Braided bundles and compact coils: The structure and thermodynamics of hexagonally packed chiral filament assemblies. *Phys. Rev. E* **79**, 041919 (2009).
33. G. M. Grason, Colloquium: Geometry and optimal packing of twisted columns and filaments. *Rev. Mod. Phys.* **87**, 401–419 (2015).
34. C. P. Broedersz *et al.*, Cross-link-governed dynamics of biopolymer networks. *Phys. Rev. Lett.* **105**, 238101 (2010).
35. K. W. Müller *et al.*, Rheology of semiflexible bundle networks with transient linkers. *Phys. Rev. Lett.* **113**, 049901 (2014).
36. A. D. Doyle, Generation of 3D collagen gels with controlled diverse architectures. *Curr. Protoc. Cell Biol.* **72**, 10.20.1–10.20.16 (2016).
37. E. Reissner, On finite deformations of space-curved beams. *Z. Angew. Math. Phys.* **32**, 734–744 (1981).
38. J. C. Simo, A finite strain beam formulation. The three-dimensional dynamic problem. Part I. *Comput. Methods Appl. Mech. Eng.* **49**, 55–70 (1985).
39. G. Jelenic, M. A. Crisfield, Geometrically exact 3D beam theory: Implementation of a strain-invariant finite element for statics and dynamics. *Comput. Methods Appl. Mech. Eng.* **171**, 141–171 (1999).
40. C. Meier, M. J. Grill, W. A. Wall, A. Popp, Geometrically exact beam elements and smooth contact schemes for the modeling of fiber-based materials and structures. *Int. J. Solid Struct.* **154**, 124–146 (2018).
41. C. J. Cyron *et al.*, Equilibrium phase diagram of semi-flexible polymer networks with linkers. *Europhys. Lett.* **102**, 38003 (2013).
42. M. Maier *et al.*, A single charge in the actin binding domain of fascin can independently tune the linear and non-linear response of an actin bundle network. *Euro. Phys J. E* **38**, 50 (2015).
43. V. M. Slepukhin, M. J. Grill, K. W. Müller, W. A. Wall, A. J. Levine, Conformation of a semiflexible filament in a quenched random potential. *Phys. Rev.* **99**, 042501 (2019).
44. BACI: A comprehensive multi-physics simulation framework. https://baci.pages.gitlab.lrz.de/website. Accessed 24 November 2020.
45. The MathWorks Inc., MATLAB (Version R2017b, MathWorks, 2017).
46. Kitware Inc., Paraview (Version 5.8.0, Kitware, 2020).
47. Q. Hu *et al.*, Data for: Topological defects produce kinks in biopolymer filament bundles. Dryad. https://doi.org/10.7280/D1XX1C. Deposited 21 March 2021.